RESIDUAL PYRAMID ATROUS FILTERING NETWORK WITH THE ERROR LOW-RANK REPRESENTATION

Anonymous authors

000

001

002003004

010

011

012

013

014

015

016

017

018

019

021

024

025

026

027

028

029

031

033

034

035

037

040

041

042

043

044

046

047

048

049

051

052

Paper under double-blind review

ABSTRACT

Image filtering aims to eliminate perturbations and textures while preserving dominant structures, serving a pivotal role in various image processing tasks. More recently, significant advances in filtering techniques have been developed. However, existing approaches typically suffer from oversmoothing edges, gradient reversal, and halos. Such issues originate from the difficulty in striking an optimal tradeoff between filtering multi-scale textures and preserving edges. Furthermore, deep learning-based filtering frameworks lack modules designed to capture features of different long-range dependence textures. Consequently, the task of filtering textures while maintaining edge integrity continues to pose a significant challenge. To address these issues, we propose a novel residual pyramid atrous filtering network (RPAFNet) that utilizes the error low-rank representation. Specifically, we introduce a lightweight dilated spatial convolution (LDSC) module for effectively extracting multi-scale texture features. To boost the reconstruction feature space, we propose a difference residual layer (DRL) module for connecting the encoder and decoder. Additionally, by employing low-rank approximation, we introduce a new non-convex optimization model, termed gradient error low-rank representation model (GELR), which effectively suppresses textures and preserves edges. This paper provides complete theoretical derivations for solving GELR and its convergence. Extensive experiments demonstrate that the proposed approach outperforms previous techniques in attaining an equilibrium between texture filtering and edge retention, as validated by both visual comparison and quantitative evaluation across various smoothing and downstream applications.

1 Introduction

Texture filtering is a core technique in computer graphics and vision, with applications ranging from detail enhancement (Zhong et al., 2023a) and compression artifact removal (Long et al., 2025) to tone mapping (Zhu et al., 2019). Its main objective is to suppress texture while preserving structural edges. However, the diversity and complexity of textures make this a persistent challenge. Existing methods fall into three main categories: local filtering (Gavaskar & Chaudhury, 2018), global optimization (He et al., 2023), and deep learning-based approaches (Shang et al., 2024). Local filters (Cho et al., 2014; Tomasi & Manduchi, 1998; Zhang et al., 2014a) use weighted pixel relationships to achieve image smoothing. However, since they have a fixed filter size, they often suffer from staircase artifacts, halo effects, and being unadaptive to multi-scale textures, like RGF (Zhang et al., 2014b) and MuGIF (Guo et al., 2018). Global optimization methods (Gudkov & Moiseev, 2020; He et al., 2023) typically convert the filtering task into a global optimization problem, which often has high computational costs. They struggle with multi-scale textures and also suffer from gradient reversal and halo artifacts. Deep learning approaches (Lu et al., 2018; Shang et al., 2024) leverage neural networks to learn feature representation from data to reconstruct smoothed images. These networks are limited to local information in filtering tasks. This hampers their ability to handle multi-scale textures. Figure 1 shows the case of handling multi-scale textures of existing approaches.

To address the challenge of handling multi-scale textures and preserving edges, we propose a novel residual pyramid atrous filtering network (RPAFNet) with the low-rank representation. Specifically, to extract multi-scale features, we introduce a lightweight dilated spatial convolution (LDSC) module to expand the receptive field, enabling the network to capture global and long-range texture information. To enhance the reconstruction feature space, we propose a difference residual layer (DRL)

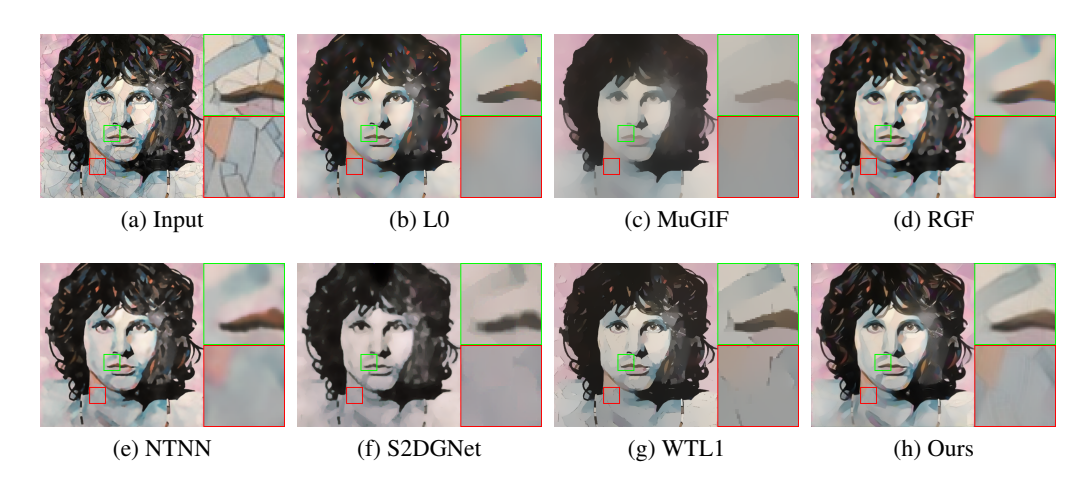


Figure 1: Comparison of handling multi-scale textures. (a) Input, smoothed results of (b) L0, (c) MuGIF, (d) RGF, (e) NTNN, (f) S2DGNet, (g) WTL1, and (h) Ours. It is hard to balance multi-scale texture removal and structural preservation for competing algorithms.

module in the proposed network. Finally, to overcome the over-smoothing edges and effectively suppress textures, we introduce a novel non-convex optimization filtering model with the error low-rank representation, which dynamically constrains the RPAFNet to preserve structural information. In a nutshell, the primary contributions of this work are concluded as follows: (1) We introduce the novel RPAFNet, including the proposed LDSC and DRL modules, which ensure effective handling of multi-scale and enhance the feature space for the reconstruction stage. (2) We propose a non-convex optimization model that utilizes a low-rank representation of the error map. The non-convex model dynamically constrains the RPAFNet to achieve texture removal and edge preservation. (3) Extensive experimental results demonstrate that our model outperforms state-of-the-art techniques in both visual quality and numerical performance across diverse smoothing applications.

Theoretical convergence derivations and additional downstream smoothing application experiments that have been omitted for space appear in the Appendix material.

2 Related Work

Local Filters. Local filters smooth images by using nearby texture and structure information. Bilateral filtering (Tomasi & Manduchi, 1998), which weights neighboring pixels with Gaussian kernels, often causes gradient reversals and halo artifacts. Joint bilateral filtering (Cho et al., 2014) focus on low-structure regions to better extract textures. Edge-aware techniques (Xu & Wang, 2018) enhance structure preservation by incorporating edge weights. Recent advancements further refine window design and feature modeling: edge-aware windows reduce boundary interference (Xu & Wang, 2019), dynamic windows prevent texture-structure overlap (Pradhan & Patra, 2024), and histogrambased approaches improve texture-structure separation (Liu et al., 2020b). However, local filters rely on nearby pixel information, they struggle with multi-scale textures.

Model Based Methods. These algorithms formulate image smoothing as a global optimization problem, where data terms maintain similarity to the original image and regularization terms control texture suppression. Total variation (TV) (Rudin et al., 1992) minimizes image gradients to achieve smoothing but struggles with complex textures. Weighted least squares (WLS) (Farbman et al., 2008a) reduce artifacts more effectively but can introduce color shifts. Gradient minimization (Xu et al., 2011) controls non-zero gradients for improved smoothing. Relative total variation (RTV) (Xu et al., 2012) separates texture and structure via relative variation. Various prior-guided iterative methods have emerged. Locally adaptive models (Farbman et al., 2008a) and truncated Huber penalties (Li & Li, 2023) offer greater control over smoothing behavior. However, these methods still face challenges in balancing multi-scale texture smoothing and edge preservation, leading to the suffering from gradient reversal and halo artifacts.

Learning Based Methods. These approaches utilize neural networks for filtering that are typically categorized into two main types: supervised and unsupervised methods. Supervised models relied

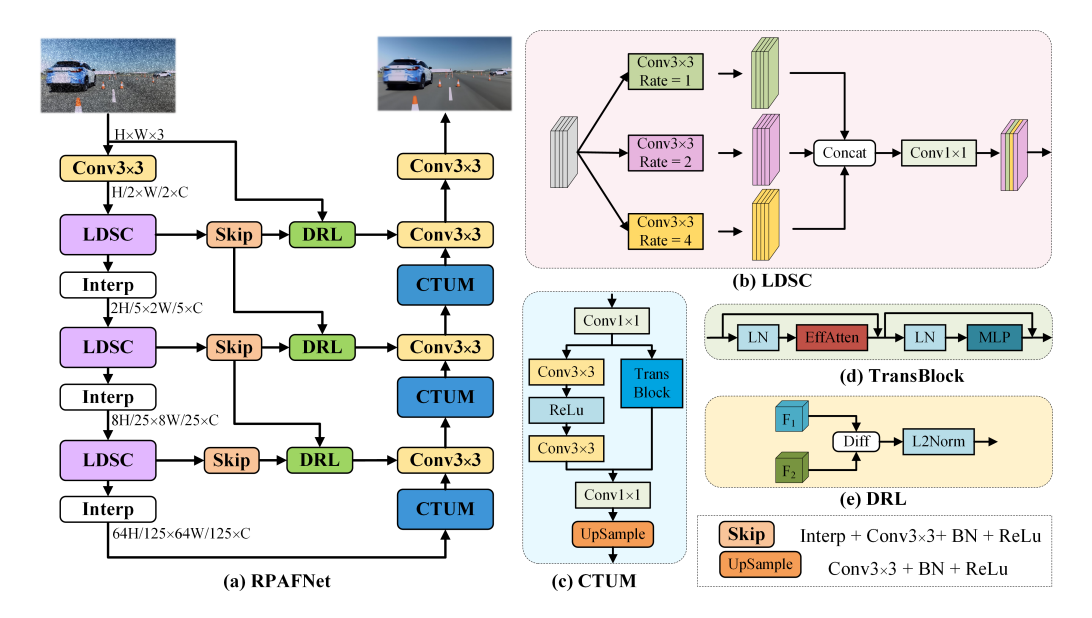


Figure 2: Main workflow of our proposed technique. (a) Main architecture of the Residual Pyramid Atrous Filtering Network (RPAFNet). (b) Structure of LDSC module, (c) Structure of CTUM module, (d) TransBlock module, (e) Structure of DRL module.

on ground truth data, such as attention-aware filters (Zhong et al., 2023b) and fully convolutional networks with large receptive fields (Chen et al., 2017b). E2H (Feng et al., 2021) improves results by jointly performing edge detection and structure-preserving smoothing using a tailored total variation loss. To reduce dependence on paired datasets, unsupervised methods emerged. Deep image prior (Ulyanov et al., 2018) uses randomly initialized networks as implicit priors. Later methods introduced input-dependent loss functions: bilateral texture loss in iterative networks (Jiang et al., 2024), weighted least squares in Deepwls (Yang et al., 2024c), and truncated norm-based regularization (Yang et al., 2024a). Despite progress, existing filtering networks lack modules for effectively extracting multi-scale texture features, limiting their effectiveness in capturing long-range dependencies.

3 METHODOLOGY

Problem Description. Given an input texture image g, and ground-truth x, we can consider the texture image to consist of image x and texture layer image T, denoted as

$$g = x + T. (1)$$

We aim to obtain the smoothed image u via the proposed network with the input texture image g, denoted as:

$$u = f_{\theta}(g). \tag{2}$$

 f_{θ} is the proposed residual pyramid atrous filtering network. However, image smoothing faces the big challenge in handling multi-scale textures. Motivated by the well-known dilated convolution (Chen et al., 2017a), we introduce a residual pyramid atrous filtering network to address this issue. To make our network capable of capturing long-range dependencies, we propose a lightweight dilated spatial convolution module to expand the receptive field in the encoder. To enrich the different levels of feature space for reconstruction, we introduce a difference residual layer module. The detailed architecture of the proposed residual pyramid atrous filtering network is shown in Figure 2. The following section introduces our designed network.

3.1 RESIDUAL PYRAMID ATROUS FILTERING NETWORK

To address the challenges posed by complex multi-scale textures, we propose a novel residual pyramid atrous filtering network, shown in Figure 2(a). RPAFNet utilizes an U-shaped architecture with a lightweight dilated spatial convolution module for encoding and a convolution transformer upsampling module for decoding. Skip connections between encoder and decoder layers are enhanced

using a difference residual layer to enrich the feature space. Downsampling is performed via the Interp module, which is a bilinear interpolation operator, progressively reducing feature size by a factor of 0.8. Upsampling in CTUM uses a 3×3 convolution layer, BatchNorm, and ReLU activation. LDSC module process features from the Interp module. Output features of LDSC undergo delta residual processing via the DRL module, which applies a subtraction operation and a L2Norm to refine details.

Lightweight dilated spatial convolution module. This model is designed for efficient feature extraction and enhanced texture awareness, as shown in Figure 2(b). The LDSC module is built based on the atrous convolution (Chen et al., 2017a), we leverage the dilated convolution (Yu & Koltun, 2016) as its unit convolution operator, as shown in Figure 2(b). This module consists of convolutional layers with varying dilation rates and scales, which is different from multi-scale dilated convolution in (Wang et al., 2019a). The LDSC module is simpler and lighter since it removes the BatchNorm and activation layers from these modules in (Chen et al., 2017a; Yu & Koltun, 2016; Wang et al., 2019a). The main differences lie in the use of 3×3 convolutional layers with dilation rates of 1, 2, and 4, followed by a concatenation operator and a 1×1 convolutional layer to unify the feature dimensions. Notably, the 3×3 convolutional layers with different dilation rates facilitate the extraction of features at different scales. This architecture allows the model to integrate multi-scale textural information.

Convolution transformer upsampling module. We propose the CTUM module to better handle image details. As shown in Figure 2(c), it processes features through two branches: a convolutional path and a Transformer path. The convolutional path uses two 3×3 convolutional layers with ReLU to extract local features. The Transformer path includes a TransBlock (Zhong et al., 2023b)(Figure 2(d)) made up of Layer Normalization (LN), Efficient Attention (EffAtten) (Shen et al., 2021), and a Multi-Layer Perceptron (MLP), along with skip connections to reduce overfitting. After both paths, features are refined using a 1×1 convolution and an upsampling module.

Difference residual layer module. This module extracts the features' differences from the previous layer and the skip layer, the architecture of which is shown in Figure 2(e). The difference map is passed to an L2Norm layer, which refers to the L_2 -norm normalization of input features. The DRL module is designed to compensate for structural information during the decoding stage, thereby reducing the loss of edges and dominant structures.

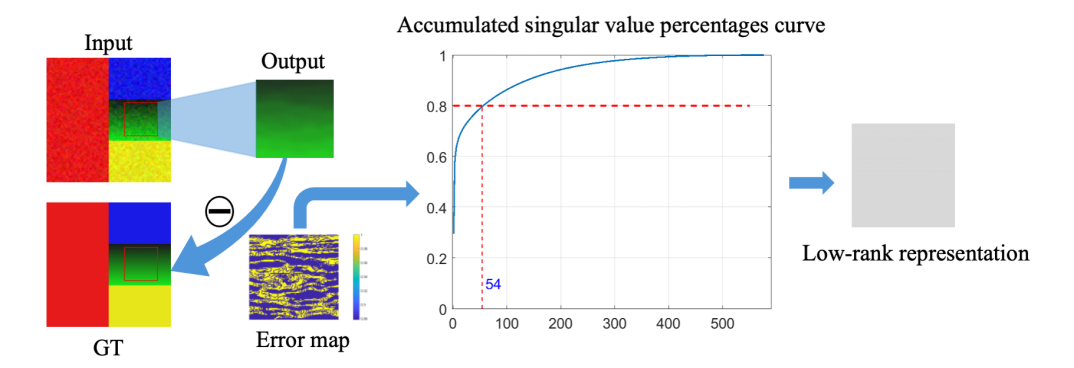


Figure 3: Pipeline of gradient error low-rank representation. The error map is the gradient error from the GT and output. And then employing a low-rank approximation on the error map suppresses textures.

3.2 Gradient error low-rank representation

To construct high-quality smoothed images, it needs to effectively filter textures and preserve edges. We aim to recover a smooth image u from the textured image g. Ideally, u is infinitely closer to x. Motivated by the merit of total variation L_1 regularization (Rudin et al., 1992; Li et al., 2025; Liu et al., 2024b) in edge preserving, we utilize $||\nabla u||_1$ regularization term to overcome the oversmoothing issue. To effectively suppress textures, we observe that low-rank approximation performs well in removing textures, which is inspired by low-rank approximation applied in denoising tasks, as shown in Figure 3. Therefore, we introduce a gradient error low-rank representation (GELR) model for integrated into the RPAFNet. It is worth noting that the gradient error is from between u and x.

In a nutshell, the proposed gradient error low-rank representation model has two items, wirtten as

$$\min_{u} \quad \alpha ||\nabla u||_1 + \beta ||\nabla u - \nabla x||_r, \quad \text{s.t.} \quad g = u + T.$$
 (3)

 α , β are positive penalty parameters. The second item is the low-rank approximation representation of the gradient error. r is the selected rank in approximating the gradient error map. In this study, we can adjust values of α and β to balance texture filtering and edge preservation.

To solve model equation 3, we introduce the auxiliary variables $\nabla u = d$ and $\nabla u - \nabla x = t$. The original problem equation 3 becomes

$$\min_{\substack{d \ t}} \quad \alpha ||d||_1 + \beta ||t||_r, \quad \text{s.t.} \quad g = u + T, \quad \nabla u = d, \quad \nabla u - \nabla x = t. \tag{4}$$

To address the proposed model effectively, we first introduce a key definition and a fundamental theorem.

Definition 3.1 (Truncated Nuclear Norm (Chen et al., 2024)). Given a matrix $Z \in \mathbb{R}^{m \times n}$, the truncated nuclear norm $||Z||_r$ is defined as:

$$||Z||_r = \sum_{i=r+1}^{\min\{m,n\}} \sigma_i(Z),$$
 (5)

where $r = \lfloor \theta \min(m, n) \rfloor$, $\lfloor \cdot \rfloor$ denotes the largest integer that is less than or equal to input value. θ is the truncated rate, σ_i denotes the singular values.

The truncated nuclear norm cannot be solved directly due to its non-convexity. Based on the analysis in (Xue et al., 2019), assuming that Z has a singular value decomposition $Z = U\Sigma V^T$, where $U = (u_1, \cdots, u_m) \in \mathbb{R}^{m \times m}$, $\Sigma \in \mathbb{R}^{m \times n}$, and $V = (v_1, \cdots, v_n) \in \mathbb{R}^{n \times n}$. Therefore, the trunctated nuclear norm can become

$$||Z||_r = ||Z||_* - \max[\text{Tr}(AZB^t)], \quad \text{s.t.} \quad AA^T = I, \quad BB^T = I.$$
 (6)

 $A=(u_1,\cdots,u_r)^T\in\mathbb{R}^{r\times m}$ and $B=(v_1,\cdots,v_r)^T\in\mathbb{R}^{r\times n}$. $I\in\mathbb{R}^{r\times r}$ denotes the unit matrix. $Tr(\cdot)$ is the trace. We present the detailed derivation process in **appendix A.1**.

Theorem 3.2. (Xue et al., 2019) For any given matrix $Q \in \mathbb{R}^{m \times n}$ with rank r. Then, the following problem has a unique closed-form solution, denoted as:

$$Z_* = \arg\min_{Z} \mu ||Z||_* + \frac{1}{2}||Z - Q||_2^2.$$
 (7)

It takes the form

$$Z_* = SVT_{u.r}(Q) \in \mathbb{R}^{m \times n},\tag{8}$$

where $SVT_{\mu,r}(\cdot)$ is defined by

$$SVT_{\mu,r}(Q) = Udiag([\max(\sigma - \mu, 0)])V^T, \tag{9}$$

where $U \in \mathbb{R}^{m \times r}$, $V \in \mathbb{R}^{r \times n}$, and $\sigma = (\sigma_1, \sigma_2, \sigma_3, \dots, \sigma_r)^T \in \mathbb{R}^r$, which are obtained via the Singular Value Decomposition of Q. That means $Q = U \operatorname{diag}(\sigma) V^T$. The detailed proof, see (Xue et al., 2019).

3.3 OPTIMIZATION ALGORITHM

In this work, we use an alternating direction method of multipliers (ADMM) to solve the proposed model equation 4. The corresponding augmented Lagrange function is written as:

$$\mathcal{L}(u, d, t, \eta_d, \eta_t, T) = \frac{1}{2} ||g - u - T||_2^2 + \alpha ||d||_1 + \frac{\rho_1}{2} ||\nabla u - d + \eta_d||_2^2 + \beta ||t||_r + \frac{\rho_2}{2} ||\nabla u - \nabla x - t + \eta_t||_2^2,$$
(10)

where η_d and η_t are Lagrange multipliers, ρ_1 , ρ_2 are Lagrange parameters. We split objective function equation 10 into the following subproblems, which means solving model equation 4 is

equivalent to solving equation 10 via iterative scheme. The all subproblems are listed as follows:

$$\begin{cases} u^{k+1} = \arg\min_{u} ||g - u - T^{k}||_{2}^{2} + \frac{\rho_{1}}{2} ||\nabla u - d^{k} + \eta_{d}^{k}||_{2}^{2} + \frac{\rho_{2}}{2} ||\nabla u - \nabla x - t^{k} + \eta_{t}^{k}||_{2}^{2}, \\ d^{k+1} = \arg\min_{d} \alpha ||d||_{1} + \frac{\rho_{1}}{2} ||\nabla u^{k+1} - d + \eta_{d}^{k}||_{2}^{2}, \\ t^{k+1} = \arg\min_{t} \beta ||t||_{r} + \frac{\rho_{2}}{2} ||\nabla u^{k+1} - \nabla x - t + \eta_{t}^{k}||_{2}^{2}, \\ \eta_{d}^{k+1} = \eta_{d}^{k} + (\nabla u^{k+1} - d^{k+1}), \\ \eta_{t}^{k+1} = \eta_{t}^{k} + (\nabla u^{k+1} - \nabla x - t^{k+1}), \\ T^{k+1} = g - u^{k+1}, \end{cases}$$

$$(11)$$

where k denotes the iteration number. Each subproblem is discussed in **appendix A.2**.

To ensure our designed network to learning texture and edge features, we utilize the proposed model to dynamically constrain RPAFNet training. Therefore, for solving the *u*-subproblem,

$$u^{k+1} = \arg\min_{u} ||g - u - T^k||_2^2 + \frac{\rho_1}{2} ||\nabla u - d^k + \eta_d^k||_2^2 + \frac{\rho_2}{2} ||\nabla u - \nabla x - t^k + \eta_t^k||_2^2.$$
 (12)

We exploit the output of the proposed neural network to update u, meaning that $u^{k+1} = f_{\theta}(g)$. It is evident that equation 12 can be rewritten as a loss function, denoted as

$$\mathcal{L}_{1} = ||g - f_{\theta}(g) - T^{k}||_{2}^{2} + \frac{\rho_{1}}{2}||\nabla f_{\theta}(g) - d^{k} + \eta_{d}^{k}||_{2}^{2} + \frac{\rho_{2}}{2}||\nabla f_{\theta}(g) - \nabla x - t^{k} + \eta_{t}^{k}||_{2}^{2}, \quad (13)$$

where f_{θ} represent the proposed neural network. \mathcal{L}_1 is one part of our total loss function, we also take the \mathcal{L}_2 loss, which is written as

$$\mathcal{L}_2 = ||f_{\theta}(g) - x||_2^2 + SSIM(f_{\theta}(g), x), \tag{14}$$

where the SSIM is the structural similarity index. The total loss function is

$$\mathcal{L} = \lambda_1 \mathcal{L}_1 + \lambda_2 \mathcal{L}_2. \tag{15}$$

 λ_1 and λ_2 are two positive constants. The dynamic iterative strategy for constraining RPAFNet to training ensures the flexibility of our network's smoothing strength. The solution to each subproblem, computational complexity, and detailed global convergence proof of the non-convex optimization algorithm are presented in **appendix A.4**.

4 EXPERIMENTS

4.1 SETTINGS AND DATASETS

Setings. The proposed RPAFNet was driven to training via the proposed low-rank representation model, whose loss function is defined in equation 15 with $\lambda_1=0.7, \lambda_2=0.3$. Initially, parameters α , β are experimentally set to 0.4, 0.6, respectively. While ρ_1, ρ_2 are assigned to 1 theoretically. Input images are resized into 512×512 . We set the epoch number as 200, and batchsize is set to 4. The RPAFNet is updated via Adam optimizer with a learning rate 0.001. All experiments are conducted using PyTorch on a Ubuntu 20.04 server with two RTX 4090 GPUs. Our code will be available on github.

Datasets. We utilize the SPS (Feng et al., 2021) dataset to train RPAFNet, and compare performance on NKS(Xu et al., 2020) and ECS (Qi et al., 2024) datasets, which all have paired ground-truth smoothed images. Smoothing performance was assessed using PSNR and SSIM across the three datasets. We also utilized no-reference metrics: BRISQE (Mittal et al., 2012a), NIQE (Mittal et al., 2012b), PIQE (Venkatanath et al., 2015), ILNIQE (Zhang et al., 2015), and BLIINDS2 (Saad et al., 2012) to further evaluate performance for test images without paired ground-truth.

4.2 RESULTS ANALYSIS

We present a comparative analysis against state-of-the-art filtering techniques, including ILS (Liu et al., 2020a), L0 (Xu et al., 2011), L0L1 (Yang et al., 2022a), L1E (Yang et al., 2022b), PTF (Zhang et al., 2023), QWLS (Liu et al., 2024a), SEMF (Huang et al., 2023), WLS (Farbman et al., 2008b), CSGIS (Wang et al., 2022), E2H (Feng et al., 2021), Deepwls (Yang et al., 2024c), NTNN (Zhu et al., 2024), S2DGNet (Qi et al., 2024), and WTL1 (Yang et al., 2024b). For non-deep traditional methods, hyperparameters are configured according to the settings reported in their original papers

326327328

342

343

344

345 346

347

348

349

350

351

352

353

354

355

356

357

359

360

361

362

364

365

366

367 368

369

370

371

372

373 374

375

376

377

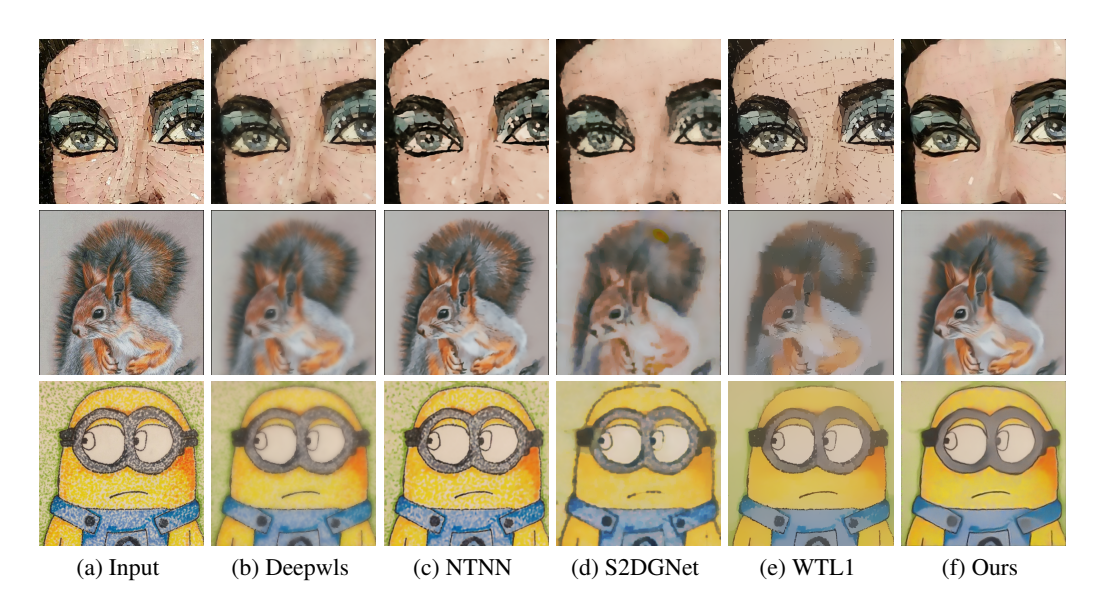


Figure 4: Image filtering for competing approaches. Results of (a) input images, (b) Deepwls, (c) NTNN, (d) S2DGNet, (e) WTL1, (f) Ours, respectively. It is evident that the proposed model obtains the best visual effects.

and tuned to enhance performance. We utilize pre-trained models released by authors for deep learning-based approaches.

Figure 4 and Table 1 show results of different methods on three real-world images. RPAFNet outperforms current state-of-the-art methods in removing textures while preserving edges. In the first row of Figure 4, Deepwls, NTNN, and WTL1 fail to remove textures effectively. S2DGNet performs better, but our method produces the best visual results. In the second and third rows, Deepwls over-smooths the images, and NTNN fails in these two cases. S2DGNet and WTL1 also struggle to preserve edges. In contrast, our method achieves both effective smoothing and structure preservation. Table 1 reports four no-reference quality metrics, where RPAFNet consistently achieves the top scores.

NIQE ↓ **ILNIQE** ↓ Methods **BRISQUE PIQE** ↓ Mean ↓ L0L1 (2022) 60.899 7.916 75.196 58.167 50.545 PTF (2023) 40.235 6.128 72.312 27.167 36.461 81.209 QWLS (2024) 44.581 5.448 35.500 41.685 46.798 CSGIS (2022) 28.528 4.694 14.333 23.588 64.916 E2H (2021) 31.587 4.530 28.333 32.342 Deepwls (2023) 51.011 5.057 82.439 31.833 42.585 NTNN (2024) 43.225 5.021 80.325 42.000 42.643 47.969 WTL1 (2024) 50.419 7.583 81.208 52.667 Ours 19.725 4.491 46.768 12.333 20.829

Table 1: No-reference metric values on Figure 4.

To demonstrate RPAFNet strong edge-preservation ability, we present enlarged areas and their corresponding 1D smoothed signals in Figure 5. The blue line represents the input signal, and the red line shows the smoothed result. Key areas are highlighted with red arrows. CSGIS and E2H fail to remove textures cleanly. Deepwls, NTNN, and WTL1 overly filter edges, as seen in the peaks marked by the first arrows. S2DGNet performs reasonably well but introduces staircase artifacts. In contrast, our method effectively removes textures while preserving sharp and clean edges.

4.3 ABLATION STUDY

LDSC module. To evaluate the effectiveness of the LDSC module in handling multi-scale textures, we perform an ablation study, as shown in Figure 6. Without the LDSC module, the baseline network struggles to remove multi-scale textures as shwon in Figure 6(b). It still contains noticeable



Figure 5: Texture removal comparisons. (a) The input image, results of (b) CSGIS, (c) E2H, (d) Deepwls, (e) NTNN, (f) S2DGNet, (g) WTL1, and (h) Ours. The right-bottom part of each image is the 1D signal smoothed result corresponding to the yellow line in the green marked box. The blue line is the input 1D signal, while the red is the smoothed result. We note that our method has a better-smoothed output than other techniques. Meanwhile, the proposed model keeps better edges.

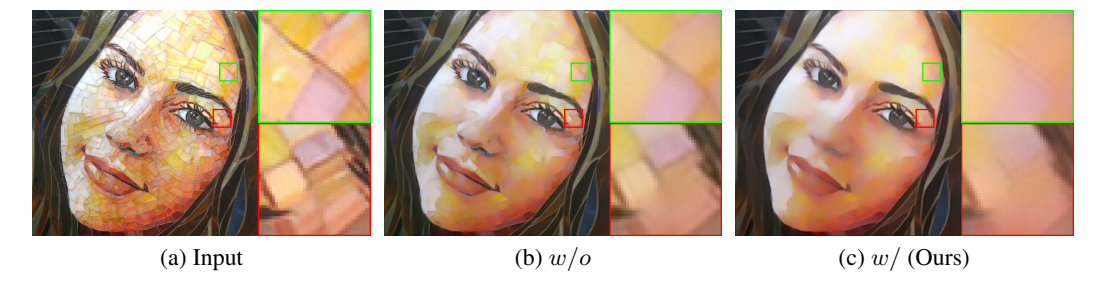


Figure 6: Ablation study on the LDSC module. (a) The input image, (b) w/o denotes the baseline network without LDSC module, while (c) w/ denotes our full network. The significant effects of the LDSC module on textures can be seen in these enlarged areas.

Table 2: No-reference metrics on the LDSC module ablation study.

Methods	Metrics	BRISQUE ↓	PIQE ↓	ILNIQE ↓
Baseline	w/o	29.786	45.096	21.000
Ours	w/	27.086	35.568	17.500

textures, referring to highlighted and enlarged regions. In contrast, RPAFNet successfully removes these textures, as illustrated in Figure 6(c). Meanwhile, Table 2 reports no-reference quality metrics corresponding to this ablation study. Both the visual results and metric values demonstrate the LDSC module effectiveness in smoothing multi-scale textures.

DRL module. We conduct an ablation study to validate the capability of the DRL module in enriching the feature space for reconstruction, as shown in Figure 7. The output from RPANet retains more fine details than that of the baseline network, achieving a PSNR of 27.43 and an SSIM of 0.9065. Both the visual results and quantitative metrics indicate that the DRL module enhances the feature space, allowing for the preservation of more content.

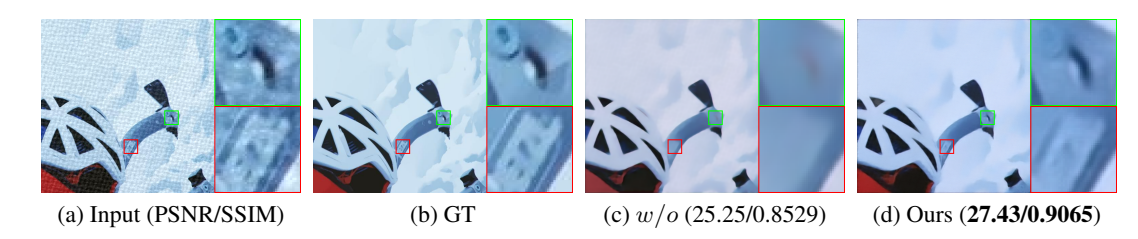


Figure 7: Ablation experiments for the DRL module. (a) Input (b) GT, (c) w/o denotes smoothed result of removing DRL module in the proposed network, (d) smoothed image of RPANet. Full network obtains the best index values and visual effects.

Table 3: No-reference metrics on loss functions ablation study.

Methods	Metrics	BRISQUE ↓	PIQE ↓	BLIINDS2 ↑
Baseline	$\lambda_1 = 0$	30.457	44.326	33.963
RPAFNet	$\lambda_1 \neq 0$	21.172	37.514	52.748

Parameters λ_1, λ_2 and α, β . We have confirmed the parameters' impact on smoothing performance by ablation studies. Experimental results of $\lambda_1=0$ have been reported in Table 3. The \mathcal{L}_1 loss is optimized iteratively using the ADMM algorithm, whereas \mathcal{L}_2 is directly optimized within an end-to-end framework. Thus, evaluating \mathcal{L}_1 also implicitly assesses the impact of the optimization algorithm, whose corresponding visual comparison and different values of λ_1, λ_2 have been shown in **appendix B.** To confirm the values of α, β , we have conducted a series of experiments for each of them from 0.1 to 1.0. Quantitative numerical results are shown in Table 4.

Table 4: Quantitative results of different values for α, β .

(α, β)	(0.1,0.9)	(0.2,0.8)	(0.3,0.7)	(0.4,0.6)	(0.5,0.5)
BRISQUE↓	49.761	45.746	35.075	27.448	29.539
$\mathbf{NIQE}\downarrow$	7.593	6.219	5.827	4.692	5.146
(α,β)	(0.6,0.4)	(0.7,0.3)	(0.8,0.2)	(0.9,0.1)	(1.0,0)
BRISQUE↓	30.471	35.841	38.775	41.577	45.381
NIQE↓	4.922	5.792	6.933	7.891	10.273

CTUM module. CTUM module enables the fusion of both local and global representations, thereby enriching the feature space. We conduct an ablation study to confirm its reconstruction performance in the deconder stage, as shown in **appendix B**. The best index values demonstrate that the CTUM module effectively preserves image fines.

5 CONCLUSIONS AND LIMITATTIONS

This work introduces a novel smoothing network with integrates gradient error low-rank representation, named the residual pyramid atrous filtering network (RPAFNet). The LDSC module serves as a tool for effectively extracting multi-scale texture features. The proposed DRL module enhances the reconstruction feature space to enable RPAFNet to keep essensail fines. We introduce a novel non-convex gradient error low-rank representation model for dynamically constraining RPAFNet to learning discrimination between textures and edges. The solution of the proposed model is supported by a complete theoretical guarantee with the ADMM algorithm. Extensive experiments, including smoothing and downstream applications, demonstrate that RPAFNet outperforms state-of-the-art approaches in mitigating JPEG compression blocks, gradient reversal, and halos. Whether deep learning or non-deep learning filtering techniques, RPAFNet consistently achieves a superior balance between filtering multi-scale textures and edge preservation.

Limitations. Supervised deep learning-based filtering techniques, including our RPAFNet, have a common limitation: their performance upper is limited by training pairs. A promising direction for future work would be to design a self-supervised framework for filtering multi-scale textures. Meanwhile, although our RPAFNet achieves superior performance in handling multi-scale textures, it has constraints when dealing with low contrast textures, which means texture color close to that of the background. Exploring the potential of different color space types' impact could provide valuable insights into achieving more effective texture filtering while maintaining edges.

REFERENCES

- Jérôme Bolte, Shoham Sabach, and Marc Teboulle. Proximal alternating linearized minimization for nonconvex and nonsmooth problems. *Mathematical Programming*, 146(1):459–494, 2014.
- Liang-Chieh Chen, George Papandreou, Iasonas Kokkinos, Kevin Murphy, and Alan L Yuille. Deeplab: Semantic image segmentation with deep convolutional nets, atrous convolution, and fully connected crfs. *IEEE transactions on pattern analysis and machine intelligence*, 40(4): 834–848, 2017a.
- Peng Chen, Fang Li, Deliang Wei, and Changhong Lu. Low-rank and deep plug-and-play priors for missing traffic data imputation. *IEEE Transactions on Intelligent Transportation Systems*, 2024.
- Qifeng Chen, Jia Xu, and Vladlen Koltun. Fast image processing with fully-convolutional networks. In *Proceedings of the IEEE International Conference on Computer Vision*, pp. 2497–2506, 2017b.
- Hojin Cho, Hyunjoon Lee, Henry Kang, and Seungyong Lee. Bilateral texture filtering. *ACM Transactions on Graphics (TOG)*, 33:1 8, 2014.
- Zeev Farbman, Raanan Fattal, Dani Lischinski, and Richard Szeliski. Edge-preserving decompositions for multi-scale tone and detail manipulation. *ACM transactions on graphics*, 27(3):1–10, 2008a.
- Zeev Farbman, Raanan Fattal, Dani Lischinski, and Richard Szeliski. Edge-preserving decompositions for multi-scale tone and detail manipulation. *ACM transactions on graphics (TOG)*, 27(3): 1–10, 2008b.
- Yidan Feng, Sen Deng, Xuefeng Yan, Xin Yang, Mingqiang Wei, and Ligang Liu. Easy2hard: Learning to solve the intractables from a synthetic dataset for structure-preserving image smoothing. *IEEE Transactions on Neural Networks and Learning Systems*, 33(12):7223–7236, 2021.
- Ruturaj G Gavaskar and Kunal N Chaudhury. Fast adaptive bilateral filtering. *IEEE transactions on Image Processing*, 28(2):779–790, 2018.
- Vladimir Gudkov and Ilia Moiseev. Image smoothing algorithm based on gradient analysis. In 2020 Ural Symposium on Biomedical Engineering, Radioelectronics and Information Technology (USBEREIT), pp. 403–406, 2020.
- Xiaojie Guo, Yu Li, Jiayi Ma, and Haibin Ling. Mutually guided image filtering. *IEEE Transactions on Pattern Analysis and Machine Intelligence*, 42(3):694–707, 2018.
- Lei He, Zhaohui Jiang, Yongfang Xie, and Zhipeng Chen. Structure-preserving texture smoothing with scale-aware intensity aggregation structure measurement. *Digital Signal Processing*, 136: 103991, 2023.
- Ruizhi Hou and Fang Li. Hyperspectral image denoising via cooperated self-supervised cnn transform and nonconvex regularization. *Neurocomputing*, 616:128912, 2025.
- Yao Hu, Debing Zhang, Jieping Ye, Xuelong Li, and Xiaofei He. Fast and accurate matrix completion via truncated nuclear norm regularization. *IEEE transactions on pattern analysis and machine intelligence*, 35(9):2117–2130, 2012.
- Junqing Huang, Haihui Wang, Xuechao Wang, and Michael Ruzhansky. Semi-sparsity for smoothing filters. *IEEE Transactions on Image Processing*, 32:1627–1639, 2023.
- Lixi Jiang, Xujie Li, and Yandan Wang. Iterative unsupervised deep bilateral texture filtering. *The Visual Computer*, 40(5):3055–3067, 2024.
- Fang Li and Tingting Li. A truncated generalized huber prior for image smoothing. *Applied Mathematical Modelling*, 123:332–347, 2023.
 - Yuemei Li, Guojia Hou, Peixian Zhuang, and Zhenkuan Pan. Dual high-order total variation model for underwater image restoration. *IEEE Transactions on Multimedia*, 2025.

- Wei Liu, Pingping Zhang, Xiaolin Huang, Jie Yang, Chunhua Shen, and Ian Reid. Real-time image smoothing via iterative least squares. *ACM Transactions on Graphics (TOG)*, 39(3):1–24, 2020a.
- Wei Liu, Pingping Zhang, Hongxing Qin, Xiaolin Huang, Jie Yang, and Michael Ng. Fast global image smoothing via quasi weighted least squares. *International Journal of Computer Vision*, pp. 1–30, 2024a.
 - Xingye Liu, Fen Lyu, Li Chen, Chao Li, Shaohuan Zu, and Benfeng Wang. Seismic random noise suppression based on deep image prior and total variation. *IEEE Transactions on Geoscience and Remote Sensing*, 62:1–11, 2024b.
 - Yang Liu, Guangda Liu, Hongliang Liu, and Changying Liu. Structure-aware texture filtering based on local histogram operator. *IEEE Access*, 8:43838–43849, 2020b.
 - Jianwu Long, Shuang Chen, Kaixin Zhang, Yuanqin Liu, Qi Luo, and Yuten Chen. Global sparse texture filtering for edge preservation and structural extraction. *Computers & Graphics*, 128: 104213, 2025.
 - Kaiyue Lu, Shaodi You, and Nick Barnes. Deep texture and structure aware filtering network for image smoothing. In *Proceedings of the European conference on computer vision (ECCV)*, pp. 217–233, 2018.
 - Anish Mittal, Anush Krishna Moorthy, and Alan Conrad Bovik. No-reference image quality assessment in the spatial domain. *IEEE Transactions on Image Processing*, 21(12):4695–4708, 2012a.
 - Anish Mittal, Rajiv Soundararajan, and Alan C Bovik. Making a completely blind image quality analyzer. *IEEE Signal processing letters*, 20(3):209–212, 2012b.
 - René Poliquin and R Rockafellar. Prox-regular functions in variational analysis. *Transactions of the American Mathematical Society*, 348(5):1805–1838, 1996.
 - Kunal Pradhan and Swarnajyoti Patra. Semantic-aware structure-preserving median morpho-filtering. *The Visual Computer*, 40(2):505–521, 2024.
 - Huiqing Qi, Shengli Tan, and Xiaoliu Luo. Self-supervised dual generative networks for edge-preserving image smoothing. In *IEEE International Conference on Acoustics, Speech and Signal Processing*, pp. 7215–7219, 2024.
 - Leonid I Rudin, Stanley Osher, and Emad Fatemi. Nonlinear total variation based noise removal algorithms. *Physica D: nonlinear phenomena*, 60(1-4):259–268, 1992.
 - Michele A Saad, Alan C Bovik, and Christophe Charrier. Blind image quality assessment: A natural scene statistics approach in the dct domain. *IEEE Transactions on Image Processing*, 21(8):3339–3352, 2012.
 - Wanqing Shang, Guojun Liu, Yazhen Wang, Jianjun Wang, and Yuemei Ma. A non-convex low-rank image decomposition model via unsupervised network. *Signal Processing*, 223:109572, 2024.
 - Zhuoran Shen, Mingyuan Zhang, Haiyu Zhao, Shuai Yi, and Hongsheng Li. Efficient attention: Attention with linear complexities. In *Proceedings of the IEEE/CVF winter conference on applications of computer vision*, pp. 3531–3539, 2021.
 - Carlo Tomasi and Roberto Manduchi. Bilateral filtering for gray and color images. In *Sixth international conference on computer vision*, pp. 839–846, 1998.
 - Dmitry Ulyanov, Andrea Vedaldi, and Victor Lempitsky. Deep image prior. pp. 9446–9454, 2018.
 - Narasimhan Venkatanath, D Praneeth, Maruthi Chandrasekhar Bh, Sumohana S Channappayya, and Swarup S Medasani. Blind image quality evaluation using perception based features. In *The first national conference on communications*, pp. 1–6, 2015.
 - Jie Wang, Yongzhen Wang, Yidan Feng, Lina Gong, Xuefeng Yan, Haoran Xie, Fu Lee Wang, and Mingqiang Wei. Contrastive semantic-guided image smoothing network. In *Computer Graphics Forum*, number 41-7, pp. 335–346, 2022.

- Yanjie Wang, Guodong Wang, Chenglizhao Chen, and Zhenkuan Pan. Multi-scale dilated convolution of convolutional neural network for image denoising. *Multimedia Tools and Applications*, 78:19945–19960, 2019a.
 - Yu Wang, Wotao Yin, and Jinshan Zeng. Global convergence of admm in nonconvex nonsmooth optimization. *Journal of Scientific Computing*, 78:29–63, 2019b.
 - Jun Xu, Zhi-Ang Liu, Ying-Kun Hou, Xian-Tong Zhen, Ling Shao, and Ming-Ming Cheng. Pixellevel non-local image smoothing with objective evaluation. *IEEE Transactions on Multimedia*, 23:4065–4078, 2020.
 - Li Xu, Cewu Lu, Yi Xu, and Jiaya Jia. Image smoothing via 10 gradient minimization. In *Proceedings of the 2011 SIGGRAPH Asia conference*, pp. 1–12, 2011.
 - Li Xu, Qiong Yan, Yang Xia, and Jiaya Jia. Structure extraction from texture via relative total variation. *ACM Trans. Graph.*, 31(6):1–10, 2012.
 - Panpan Xu and Wencheng Wang. Improved bilateral texture filtering with edge-aware measurement. *IEEE Transactions on Image Processing*, 27(7):3621–3630, 2018.
 - Panpan Xu and Wencheng Wang. Structure-aware window optimization for texture filtering. *IEEE Transactions on Image Processing*, 28(9):4354–4363, 2019.
 - Zhichao Xue, Jing Dong, Yuxin Zhao, Chang Liu, and Ryad Chellali. Low-rank and sparse matrix decomposition via the truncated nuclear norm and a sparse regularizer. *the visual computer*, 35 (11):1549–1566, 2019.
 - Yang Yang, Ling Tang, Lanling Zeng, Xinyu Wang, and Yongzhao Zhan. L0 image smoothing via iterating truncated 11 gradient regularization. *Journal of Electronic Imaging*, 31(5):053016–053016, 2022a.
 - Yang Yang, Hao Zheng, Lanling Zeng, Xiangjun Shen, and Yongzhao Zhan. L1-regularized reconstruction model for edge-preserving filtering. *IEEE Transactions on Multimedia*, 25:4148–4162, 2022b.
 - Yang Yang, Ling Tang, Tao Yan, Lanling Zeng, Xiangjun Shen, and Yongzhao Zhan. Parameterized 10 image smoothing with unsupervised learning. *IEEE Transactions on Emerging Topics in Computational Intelligence*, 8(2):1938–1951, 2024a.
 - Yang Yang, Dan Wu, Ling Tang, Lanling Zeng, and Zhigeng Pan. Weighted and truncated 11 image smoothing based on unsupervised learning. *The Visual Computer*, 40(8):5871–5882, 2024b.
 - Yang Yang, Dan Wu, Lanling Zeng, and Zhuoran Li. Weighted least square filter via deep unsupervised learning. *Multimedia Tools and Applications*, 83(11):31361–31377, 2024c.
 - Fisher Yu and Vladlen Koltun. Multi-scale context aggregation by dilated convolutions. In *The International Conference on Learning Representations*, 2016.
 - Lin Zhang, Lei Zhang, and Alan C Bovik. A feature-enriched completely blind image quality evaluator. *IEEE Transactions on Image Processing*, (8):2579–2591, 2015.
 - Qi Zhang, Xiaoyong Shen, Li Xu, and Jiaya Jia. Rolling guidance filter. In *Computer Vision–ECCV* 2014: 13th European Conference, Zurich, Switzerland, September 6-12, 2014, Proceedings, Part III 13, pp. 815–830, 2014a.
 - Qi Zhang, Xiaoyong Shen, Li Xu, and Jiaya Jia. Rolling guidance filter. In *European conference on computer vision*, pp. 815–830, 2014b.
 - Qing Zhang, Hao Jiang, Yongwei Nie, and Wei-Shi Zheng. Pyramid texture filtering. *ACM Transactions on Graphics*, 42(4):1–11, 2023.
 - Guojin Zhong, Weiping Ding, Long Chen, Yingxu Wang, and Yu-Feng Yu. Multi-scale attention generative adversarial network for medical image enhancement. *IEEE Transactions on Emerging Topics in Computational Intelligence*, 7(4):1113–1125, 2023a.

Zhiwei Zhong, Xianming Liu, Junjun Jiang, Debin Zhao, and Xiangyang Ji. Deep attentional guided image filtering. *IEEE Transactions on Neural Networks and Learning Systems*, 2023b.
Dingkun Zhu, Weiming Wang, Xue Xue, Haoran Xie, Gary Cheng, and Fu Lee Wang. Structure-preserving image smoothing via contrastive learning. *The Visual Computer*, 40(8):5139–5153, 2024.
Feida Zhu, Zhetong Liang, Xixi Jia, Lei Zhang, and Yizhou Yu. A benchmark for edge-preserving

image smoothing. IEEE Transactions on Image Processing, 28(7):3556–3570, 2019.

THE USE OF LARGE LANGUAGE MODELS

We declare that we just used the large language models to improve sentences and polish in this manuscript.

SUMMARY

This technical appendix offers a comprehensive theoretical analysis of our model, including a detailed examination of its convergence properties. Additionally, it presents both visual and numerical results for smoothing downstream tasks. The structure of this appendix is organized as follows. Section A presents a mathematical analysis of the proposed non-convex problem, which includes the derivation process of the truncated nuclear norm and numerical solution to the gradient error prior model. Meanwhile, we also analyze the convergence of the proposed optimization algorithm. Section B shows additional ablation study experimental results. Section C provides analysis of three additional application experimental results, including details manipulation, image stylization, and artifacts filtering.

A THEORETICAL ANALYSIS OF GELR MODEL

This section mainly presents the mathematical analysis on the truncated nuclear norm, solution to the non-convex optimization problem, and convergence analysis of our optimization algorithm.

A.1 DERIVATION OF TRUNCATED NUCLEAR NORM

First of all, we review the proposed non-convex optimization problem, which is denoted as:

$$\min_{d,t} \quad \alpha ||d||_1 + \beta ||t||_r,$$

s.t. $g = u + T$, $\nabla u = d$, $\nabla u - \nabla x = t$. (16)

To better analyze the proposed non-convex problem, we separate the low-rank prior terms for detailed analysis, denoted as:

$$\min_{t} \quad \beta ||t||_{r},$$
s.t.
$$\nabla u - \nabla x = t.$$
(17)

Since $||t||_r$ is non-convex, it is not easy to solve directly, then we have the following theorem (Hu et al., 2012).

Theorem A.1 ((Hu et al., 2012)). For any given matrix $X \in \mathbb{R}^{m \times n}$, any matrices $A \in \mathbb{R}^{r \times m}$, $B \in \mathbb{R}^{r \times n}$. Such that $AA^T = I_{r \times r}$, $BB^T = I_{r \times r}$. For any nonnegative integer r ($r \leq \min(m, n)$), we have

$$Tr(AXB^T) \le \sum_{i=1}^r \sigma_i(X).$$

Therefore, for the proposed model, let X = t, and then the detailed proof is as follows.

Proof. By the Von Neumann's trace inequality, we can have

$$\operatorname{Tr}(AtB^T) = \operatorname{Tr}(tB^T A) \le \sum_{i=1}^{\min(m,n)} \sigma_i(t)\sigma_i(B^T A), \tag{18}$$

where $\sigma_1(t) \geq \cdots \geq \sigma_{\min(m,n)}(t) \geq 0$. Since rank(A) = r and rank(B) = r, then $rank(B^TA) = s \leq r$. For $i \leq s$, we can get $\sigma_i(B^TA) \geq 0$. $\sigma_i^2(B^TA)$ is the *i*-th eigenvalue of $B^TAA^TB = B^TB$, which is also the eigenvalue of $BB^T = I_{r \times r}$. Therefore,

 $\sigma_i(B^TA) = 1, \forall i \geq s$, and others are 0. Thereby, we can get the follows:

$$\sum_{i=1}^{\min(m,n)} \sigma_i(t)\sigma_i(B^T A)$$

$$= \sum_{i=1}^s \sigma_i(t)\sigma_i(B^T A) + \sum_{i=s+1}^{\min(m,n)} \sigma_i(t)\sigma_i(B^T A)$$

$$= \sum_{i=1}^s \sigma_i(t) \cdot 1 + \sum_{i=s+1}^{\min(m,n)} \sigma_i(t) \cdot 0$$

$$= \sum_{i=1}^s \sigma_i(t).$$
(19)

Since $s \leq r$ and $\sigma_i(t) \geq 0$, we have

$$\sum_{i=1}^{s} \sigma_i(t) \le \sum_{i=1}^{r} \sigma_i(t). \tag{20}$$

Combining equation 18 and equation 19, we can get

$$\operatorname{Tr}(AtB^T) \le \sum_{i=1}^s \sigma_i(t) \le \sum_{i=1}^r \sigma_i(t). \tag{21}$$

Assuming that t has its singular value decomposition $t=U\Sigma V^T$, where $U=(u_1,\cdots,u_m)\in\mathbb{R}^{m\times m},\ \Sigma\in\mathbb{R}^{m\times n}$, and $V=(v_1,\cdots,v_n)\in\mathbb{R}^{n\times n}$. And when $A=(u_1,\cdots,u_r)^T$ and $B=(v_1,\cdots,v_r)^T$, we have:

$$Tr(AtB^{T}) = Tr((u_{1}, u_{2}, u_{3}, \dots, u_{r})^{T} t(v_{1}, v_{2}, v_{3}, \dots, v_{r}))$$

$$= Tr((u_{1}, u_{2}, u_{3}, \dots, u_{r})^{T} U \Sigma V^{T}(v_{1}, v_{2}, v_{3}, \dots, v_{r}))$$

$$= Tr(((u_{1}, u_{2}, u_{3}, \dots, u_{r})^{T} U) \Sigma (V^{T}(v_{1}, v_{2}, v_{3}, \dots, v_{r})))$$

$$= Tr(\begin{pmatrix} I_{r} & 0 \\ 0 & 0 \end{pmatrix} \Sigma \begin{pmatrix} I_{r} & 0 \\ 0 & 0 \end{pmatrix})$$

$$= Tr(diag(\sigma_{i}(t), \dots, \sigma_{i}(t), 0, \dots, 0))$$

$$= \sum_{i=1}^{r} \sigma_{i}(t)$$
(22)

Combining equation 21 and equation 22, we can get

$$\max_{AA^T=I,BB^T=I} \text{Tr}(AtB^T) = \sum_{i=1}^r \sigma_i(t). \tag{23}$$

Then

$$||t||_{*} - \max_{AA^{T}=I,BB^{T}=I} \text{Tr}(AtB^{T})$$

$$= \sum_{i=1}^{\min(m,n)} \sigma_{i}(t) - \sum_{i=1}^{r} \sigma_{i}(t) = \sum_{i=r+1}^{\min(m,n)} \sigma_{i}(t)$$

$$= ||t||_{r}.$$
(24)

In summary, the non-convex optimization problem equation 17 can be rewritten as

$$\underset{t}{\operatorname{arg\,min}} ||t||_{*} - \underset{AA^{T}=I,BB^{T}=I}{\operatorname{max}} \operatorname{Tr}(AtB^{T})$$
s.t. $\nabla u - \nabla x = t$. (25)

The above problem is the same as Eq.(5) of the main manuscript. Then

$$\arg \min_{t} ||t||_{*} - \max_{AA^{T} = I, BB^{T} = I} \text{Tr}(AtB^{T}) + \frac{\rho}{2} ||t - (\nabla u - \nabla x + \eta_{t})||_{2}^{2},$$
(26)

where ρ is the balance positive constant, η_t is the Lagrange multiplier. According to (Zhu et al., 2024), we can get the concise form of equation 26, denoted as

$$\arg\min_{t} ||t||_{*} + \frac{\rho}{2} ||t - (\nabla u - \nabla x + \eta_{t} - A^{T}B)||_{2}^{2}, \tag{27}$$

Therefore, we can use **Theorem 3.2** to solve the non-convex optimization problem equation 27.

A.2 NUMERICAL SOLUTION TO GELR MODEL

The proposed gradient error prior model can be expressed as the form in equation 16, we use the alternating direction method of multipliers (ADMM) to solve it. The corresponding augmented Lagrange function can be splited into subproblems, denoted as follows:

$$\begin{cases} u^{k+1} = \arg\min_{u} ||g - u - T^{k}||_{2}^{2} + \frac{\rho_{1}}{2} ||\nabla u - d^{k} + \eta_{d}^{k}||_{2}^{2} + \frac{\rho_{2}}{2} ||\nabla u - \nabla x - t^{k} + \eta_{t}^{k}||_{2}^{2}, \\ d^{k+1} = \arg\min_{d} \alpha ||d||_{1} + \frac{\rho_{1}}{2} ||\nabla u^{k+1} - d + \eta_{d}^{k}||_{2}^{2}, \\ t^{k+1} = \arg\min_{t} \beta ||t||_{r} + \frac{\rho_{2}}{2} ||\nabla u^{k+1} - \nabla x - t + \eta_{t}^{k}||_{2}^{2}, \\ \eta_{d}^{k+1} = \eta_{d}^{k} + (\nabla u^{k+1} - d^{k+1}), \\ \eta_{t}^{k+1} = \eta_{t}^{k} + (\nabla u^{k+1} - \nabla x - t^{k+1}), \\ T^{k+1} = g - u^{k+1}, \end{cases}$$

$$(28)$$

where k denotes the iteration number. Each subproblem are discussed as follows.

Update u^{k+1} by

$$u^{k+1} = \arg\min_{u} ||g - u - T^{k}||_{2}^{2} + \frac{\rho_{1}}{2} ||\nabla u - d^{k} + \eta_{d}^{k}||_{2}^{2} + \frac{\rho_{2}}{2} ||\nabla u - \nabla x - t^{k} + \eta_{t}^{k}||_{2}^{2}.$$
(29)

It is obvious that this subproblem has a closed-solution, and its first-order optimal condition is

$$T^{k} - g - \rho_1 \nabla^T (d^k - \eta_d^k) - \rho_2 \nabla^T (\nabla x + t^k - \eta_t^k)$$

+
$$(1 + \rho_1 \nabla^T \nabla + \rho_2 \nabla^T \nabla) u = 0.$$
 (30)

Then, we have

$$g - T^k + \rho_1 \nabla^T (d^k - \eta_d^k) + \rho_2 \nabla^T (\nabla x + t^k - \eta_t^k)$$

= $(1 + \rho_1 \nabla^T \nabla + \rho_2 \nabla^T \nabla) u$. (31)

According to the Fourier convolution theorem, we conduct Fourier transform on equation 31 and obtain

$$u^{k+1} = \mathcal{F}^{-1} \left(\frac{\mathcal{F}(g - T^k) + \rho_1 \mathcal{F}(\nabla^T (d^k - \eta_d^k))}{\mathcal{F}(1) + (\rho_1 + \rho_2) \mathcal{F}(\nabla^T \nabla)} \right) + \mathcal{F}^{-1} \left(\frac{\rho_2 \mathcal{F}(\nabla^T (\nabla x + t^k - \eta_t^k))}{\mathcal{F}(1) + (\rho_1 + \rho_2) \mathcal{F}(\nabla^T \nabla)} \right). \tag{32}$$

 \mathcal{F} and \mathcal{F}^{-1} denote fast Fourier transform and inverse fast Fourier transform respectively.

Update d^{k+1} by

$$d^{k+1} = \arg\min_{d} \alpha ||d||_1 + \frac{\rho_1}{2} ||\nabla u^{k+1} - d + \eta_d^k||_2^2, \tag{33}$$

The subproblem of those can be solved via the soft-thresholding skrinkage, denoted as

$$d^{k+1} = \mathbf{shrink}(\nabla u^{k+1} + \eta_d^k, \frac{1}{\rho_1}). \tag{34}$$

Algorithm 1 GELR-ADMM

Input: Image $g, x, \alpha \beta, \rho_1, \rho_2, \theta, K$. **Initialization:** $T^0, t^0, d^0, \eta_t^0, \eta_d^0 = \mathbf{0}, u^0 = g$.

- 1: **for** k = 1 : K **do**
- Update u^{k+1} via Eq. equation 32;
- Update d^{k+1} by Eq. equation 34; 3:
- Update t^{k+1} via Eq. equation 40; Update η_d^{k+1} and η_t^{k+1} via Eq. equation 41; Update T^{k+1} by Eq. equation 42;

7: end for

Output: u.

shrink function is

$$\begin{aligned} \mathbf{shrink}(\nabla u^{k+1} + \eta_d^k, \frac{1}{\rho_1}) &= \\ \mathrm{sign}(\nabla u^{k+1} + \eta_d^k) \cdot \max(|\nabla u^{k+1} + \eta_d^k| - \frac{1}{\rho_1}, 0), \end{aligned} \tag{35}$$

where $sign(\cdot)$ is the Signum function.

Update t^{k+1} by

$$t^{k+1} = \arg\min_{t} \beta ||t||_r + \frac{\rho_2}{2} ||\nabla u^{k+1} - \nabla x - t + \eta_t^k||_2^2, \tag{36}$$

according to the descriptions of **Definition 3.1** and **Theomery 3.2**, we can solve problem equation 36 via SVT_{μ,r}. Therefore, t-subproblem can be rewritten as

$$t^{k+1} = \arg\min_{t} \frac{\beta}{\rho_2} ||t||_* + \frac{1}{2} ||t - [\nabla u^{k+1} - \nabla x - t - \frac{\beta}{\rho_2} A^T B + \eta_t^k]||_2^2, \tag{37}$$

where A and B are obtained by the singular value decomposition of matrix t. Let $Q = \nabla u^{k+1}$ $\nabla x - t - \frac{\beta}{\rho_2} A^T B + \eta_t^k$, we have

$$t^{k+1} = \arg\min_{t} \frac{\beta}{\rho_2} ||t||_* + \frac{1}{2} ||t - Q||_2^2.$$
 (38)

We have the unique closed-form solution is

$$t^{k+1} = \text{SVT}_{\frac{\beta}{-},r}(Q). \tag{39}$$

Then, we have

$$t^{k+1} = \text{SVT}_{\frac{\beta}{\rho_2}, r}(Q) = U \operatorname{diag}[\max(\sigma - \frac{\beta}{\rho_2}, 0)]V^T, \tag{40}$$

where $U \in \mathbb{R}^{r \times m}$, $V \in \mathbb{R}^{r \times n}$, and $\sigma = (\sigma_1, \dots, \sigma_r)^T \in \mathbb{R}^r$ are from the Singular Value Decomposition of Q.

Update η_d^{k+1} and η_t^{k+1} by

$$\begin{cases} \eta_d^{k+1} = \eta_d^k + (\nabla u^{k+1} - d^{k+1}), \\ \eta_t^{k+1} = \eta_t^k + (\nabla u^{k+1} - \nabla x - t^{k+1}), \end{cases}$$
(41)

the two Lagrange multipliers can be updated directly.

Update T^{k+1} by

$$T^{k+1} = g - u^{k+1}, (42)$$

we obtain T^{k+1} via u^{k+1} . For completeness, the whole scheme for solving the proposed gradient error prior model with ADMM is shown in Algorithm 1.

Computational Complexity Analysis. According to the proposed optimization algorithm 1, and given an input image with size of $m \times n$, we can get the computational complexity as follows. The computational complexity of the fast Fourier transform and inverse fast Fourier transform both are $\mathcal{O}(mn\log(mn))$. The soft-thresholding shrinkage is $\mathcal{O}(mn)$, while the truncated nulcear normal and singular value decomposition are $\mathcal{O}(mn)$ and $\mathcal{O}(mnr)$, and the other subproblems are $\mathcal{O}(mn)$. Therefore, the whole algorithm 1 has a $\mathcal{O}(mnr + mn\log(mn))$ computational complexity.

SOLUTION TO GELR WITH NETWORK

First of all, we review the *u*-subproblem, denoted as:

$$u^{k+1} = \arg\min_{u} ||g - u - T^k||_2^2 + \frac{\rho_1}{2} ||\nabla u - d^k + \eta_d^k||_2^2 + \frac{\rho_2}{2} ||\nabla u - \nabla x - t^k + \eta_t^k||_2^2.$$
 (43)

To enable the model to handle multi-scale textures while giving the network better capability of adjusting smooth intensity, we consider u-subproblem as a loss function, which drives the proposed network to update and optimize parameters. And we can get u^{k+1} from trained neural network. Therefore, let $u^{k+1} = f_{\theta}(g)$. Other subproblems would have slight changes, discussed as follows.

Update d^{k+1} by the soft-thresholding skrinkage, denoted as

$$d^{k+1} = \mathbf{shrink}(\nabla f_{\theta}(g) + \eta_d^k, \frac{1}{\rho_1}). \tag{44}$$

Update t^{k+1} by $SVT_{\mu,r}$. Therefore, Let $Q = \nabla f_{\theta}(g) - \nabla x - t - \frac{\beta}{\rho_2} A^T B + \eta_t^k$, we have

$$t^{k+1} = \arg\min_{t} \frac{\beta}{\rho_2} ||t||_* + \frac{1}{2} ||t - Q||_2^2.$$
 (45)

We have the unique closed-form solution is

$$t^{k+1} = \text{SVT}_{\frac{\beta}{\rho_2}, r}(Q). \tag{46}$$

Then, we have

$$t^{k+1} = \text{SVT}_{\frac{\beta}{\rho_2}, r}(Q) = U \operatorname{diag}[\max(\sigma - \frac{\beta}{\rho_2}), 0]V^T, \tag{47}$$

where $U \in \mathbb{R}^{r \times m}$, $V \in \mathbb{R}^{r \times n}$, and $\sigma = (\sigma_1, \dots, \sigma_r)^T \in \mathbb{R}^r$ are from the Singular Value Decomposition of Q.

Update η_d^{k+1} and η_t^{k+1} by

$$\begin{cases} \eta_d^{k+1} = \eta_d^k + (\nabla f_\theta(g) - d^{k+1}), \\ \eta_t^{k+1} = \eta_t^k + (\nabla f_\theta(g) - \nabla x - t^{k+1}), \end{cases}$$
(48)

the two Lagrange multipliers can be updated directly.

Update T^{k+1} by

$$T^{k+1} = g - f_{\theta}(g), \tag{49}$$

In summary, the whole scheme for the gradient error prior guided network model is shown in Algorithm 2.

Algorithm 2 GELR with Network-ADMM

Input: Image $g, x, \alpha \beta, \rho_1, \rho_2, \theta, K$. **Initialization:** $T^0, t^0, d^0, \eta_t^0, \eta_d^0 = \mathbf{0}, u^0 = g$.

- 1: **for** k = 1 : K **do**
- Update u^{k+1} via the RPAFNet with adam;
- Update d^{k+1} by Eq. equation 44; 3:
- Update t^{k+1} via Eq. equation 47; Update η_d^{k+1} and η_t^{k+1} via Eq. equation 48; Update T^{k+1} by Eq. equation 49;
- 7: end for

Output: u.

> Computational Complexity Analysis. Since the algorithmic complexity of the neural network is related to numbers of parameters and layers, and the update of the neural network depends on the GPU, it is meaningless to calculate the algorithmic complexity. According to the proposed optimization algorithm 2, and given an input image with size of $m \times n$, we can get the computational complexity as follows. The soft-thresholding shrinkage is $\mathcal{O}(mn)$, while the truncated nulcear normal and singular value decomposition are $\mathcal{O}(mn)$ and $\mathcal{O}(mnr)$, and the other subproblems are $\mathcal{O}(mn)$. Therefore, the whole algorithm 2 has a $\mathcal{O}(mnr)$ computational complexity.

A.4 CONVERGENCE ANALYSIS

This section presents the convergence of solving GELR model with designed network. The lemma on the convergence of ADMM and some essential assumptions are from in (Wang et al., 2019b).

First of all, we provide definitions pertinent to the Lipschitz differentiable. For any function f is continuous or differentiable on its domain, we can claim that the function f is Lipschitz differentiable if it is differentiable and its gradient is Lipschitz continuous. Additionally, we need define restricted prox-regularity for regularize objetive functions and an essential Lemma.

Definition A.2 (Restricted Prox-Regularity (Wang et al., 2019b; Hou & Li, 2025)). Given a lower semi-continuous function $f: \mathbb{R}^n \to \mathbb{R} \cup \{\infty\}$, and $C \in \mathbb{R}_+$, such that

$$S_C := \{ u \in dom(f) : ||d|| > C, \forall d \in \partial f(u) \}.$$

$$(50)$$

f is called restricted prox-regular if $\forall C > 0$ and bounded set $P \subseteq dom(f)$. Then $\exists \gamma > 0$, such that

$$f(g) + \frac{\gamma}{2}||u - g||_2^2 \ge f(u) + \langle d, g - u \rangle,$$

$$\forall u \in P \setminus S_C, g \in P, d \in \partial f(u), ||d|| \le C.$$
(51)

Lemma A.3 ((Wang et al., 2019b)). Given the following general optimization problem, denoted as

$$\underset{X_k, Y}{\arg\min} f(X_0, X_1, \cdots, X_p) + h(Y), \quad \text{s.t.} \sum_{k=0}^p A_k X_K + BY = C, \tag{52}$$

where the function $f: \mathbb{R}^{n(p+1)\times m} \to \mathbb{R}$ is proper, continous, and possibly nonsmooth. While the function $h: \mathbb{R}^{q\times m} \to \mathbb{R}$ is proper and differentiable. f, h can be non-convex. Let (X^t, Y^t, Z^t) be a sequence generated by ADMM framework of equation 52. Z^t is the dual variable, μ is a psotive parameter. And \mathcal{L}_{μ} is the corresponding Lagrangian function. Assume that the following conditions hold:

A1(coercivity). Define the feasible set

$$\mathcal{F} := \left\{ (X, Y) \in \mathbb{R}^{(np+q) \times m} | AX + BY = 0 \right\},\,$$

the objective function f+h is corecive over this set, that means $f(X)+h(Y)\to\infty$ if $(X,Y)\in\mathcal{F}$ and $||(X,Y)||\to\infty$;

A2(feasibility). $Im(A) \subseteq Im(B)$, where $Im(\cdot)$ returns the image of a matrix;

A3(Lipschitz sub-minimization paths).

- (1) For any fixed X, $\arg \min_Y \{ f(X) + h(Y) | BY = U \}$ has a unique minimizer. $H: Im(B) \to \mathbb{R}^{q \times m}$ defined by $H(U) := \arg \min_Y \{ f(X) + h(Y) | BY = U \}$ is a Lipschitz continuous map.
- (2) For $k = 0, \dots, p$, we denote

$$X_{-k} := (X_0, \cdots, (X_{k-1}, (X_{k+1}, \cdots, (X_p)))$$

and for any fixed X_{-k} , Y,

$$\arg\min_{X_k} \{ f(X_k, X_{-k}) + h(Y) | A_k X_k = U \}$$

has a unique minimizer, and F_k : $Im(A_k) \to \mathbb{R}^{p \times m}$ defined by $F_k(U) := \arg \min_{X_k} \{ f(X_k, X_{-k}) + h(Y) | A_k X_k = U \}$ is a Lipschitz continuous map.

A4(objective-f regularity). f has the form $f(X) = r(X) + \sum_{k=0}^{p} f_k(X_k)$, where r(X) is Lipschitz differentiable with a constant L_r , and $f_0(X_0)$ is lower semi-continuous, $f_k(X_k)$ is restricted proxregular for $k = 1, \dots, p$;

A5(objective-h regularity). h(Y) is Lipschitz differentiable with a constant L_h ;

Specifically, if \mathcal{L}_{μ} is a Kurdyka-Łojasiewicz (KŁ) function, then for any sufficiently large μ , (X^t, Y^t, Z^t) converges globally to the unique limit point (X^*, Y^*, Z^*) , which satisfies $0 \in \mathcal{L}_{\mu}(X^*, Y^*, Z^*)$.

Upon the Lemma as mentined above, To illustrate the convergence, we need to verify that the iterative framework of our proposed algorithm satisfies the **A1-A5** in Lemma A.3 and demonstrates the KŁ property of our augmented Lagrangian function.

Proof. Suppose u can be directly obtained via $u = f_{\theta}(g)$, we rewrite the optimization problem equation 16, denoted as

$$\arg \min_{d,t} \quad \alpha \sum_{i=1}^{2} ||d_{i}||_{1} + \beta \sum_{i=1}^{2} ||t_{i}||_{r},$$
s.t. $g = u + T$, $\nabla_{i}u = d_{i}$, $\nabla_{i}u - \nabla_{i}x = t_{i}$. (53)

Let $d = [d_1, d_2]$ and $t = [t_1, t_2]$, the corresponding augmented Lagrangian function is

$$\mathcal{L}(u, d_1, d_2, t_1, t_2, \eta_d, \eta_t, T) = \frac{1}{2} ||g - u - T||_2^2 + \frac{1}{2} ||u - f_{\theta}(g)||_2^2 + \alpha \sum_{i=1}^2 ||d_i||_1$$

$$+ \frac{\rho_1}{2} ||\nabla u - d + \eta_d||_2^2 + \beta \sum_{i=1}^2 ||t_i||_r + \frac{\rho_2}{2} ||\nabla u - \nabla x - t + \eta_t||_2^2,$$
(54)

Then, we can consider f(X) as $f(X) = \alpha \sum_{i=1}^{2} ||d_i||_1$, and h(V) denotes as

$$h(V) = \beta \sum_{i=1}^{2} ||t_i||_r + \frac{1}{2}||g - u - T||_2^2 + \frac{1}{2}||u - f_{\theta}(g)||_2^2,$$

where $X=[d_1;d_2],$ and $V=[u;t_1;t_2;T].$ Therefore, we let

$$A = \begin{bmatrix} -I & 0 \\ 0 & -I \\ I & 0 \\ 0 & I \\ 0 & 0 \end{bmatrix} B = \begin{bmatrix} \nabla_1 & 0 & 0 & 0 \\ \nabla_2 & 0 & 0 & 0 \\ 0 & -I & 0 & 0 \\ 0 & 0 & -I & 0 \\ I & 0 & 0 & I \end{bmatrix} C = \begin{bmatrix} 0 \\ \nabla_1 x \\ \nabla_2 x \\ g \end{bmatrix}.$$

Suppose the gradient operators ∇_1 and ∇_2 are with zero boundary condition. Therefore, B has full column rank. In this condition, we can verify that the assumptions A1-A5 and the KŁ property hold.

The feasible set is $\mathcal{F} = \{(X, V)|AX + BV = C\}$, when $||(X, V)||_2 \to +\infty$, $f(X) + h(V) \to +\infty$. Thus **A1** holds.

Since $Im(B) = \mathbb{R}^{3mn}$, **A2** naturally holds.

In section A.3, we have presented the unique solution for each subproblem, and A, B both have full column rank with trivial null spaces. Then, we can get F and H are linear map operators. Therefore, for any $k_1, k_2 \in \mathbb{N}$, we have

$$||F_i(X^{k_1}) - F_i(X^{k_2})|| \le ||F_i||||X^{k_1} - X^{k_2}||$$

and

$$||H(V^{k_1}) - H(V^{k_2})|| \le ||H||||V^{k_1} - V^{k_2}||.$$

Thus **A3** holds.

For A4, let r = 0, $f_0 = 0$ and $f_1 = ||d||_1$, According to Examples in (Poliquin & Rockafellar, 1996). f_1 is pro-regular. Therefore, A4 naturally holds.

For A5, we have

$$h(V) = \beta \sum_{i=1}^{2} ||t_i||_r + \frac{1}{2}||g - u - T||_2^2 + \frac{1}{2}||u - f_\theta(g)||_2^2,$$

thus A5 obviously holds.

For the KŁ property of \mathcal{L}_{μ} , based on the Example 2 in (Bolte et al., 2014), \mathcal{L}_{μ} is a semi-algebratic and it satisfies the KŁ property.

Since the all conditions **A1-A5** hold and \mathcal{L}_{μ} meets the KŁ property, for any sufficiently large penalty parameters, the iterative sequence $(u^k, d_1^k, d_2^k, t_1^k, t_2^k, \eta_d^k, \eta_t^k, T^k)$ produced via the proposed GELR model with network converges globally to the unique limit point $(u^*, d_1^*, d_2^*, t_1^*, t_2^*, \eta_d^*, \eta_t^*, T^*)$ and it has $0 \in \partial \mathcal{L}_{\mu}(u^*, d_1^*, d_2^*, t_1^*, t_2^*, \eta_d^*, \eta_t^*, T^*)$.

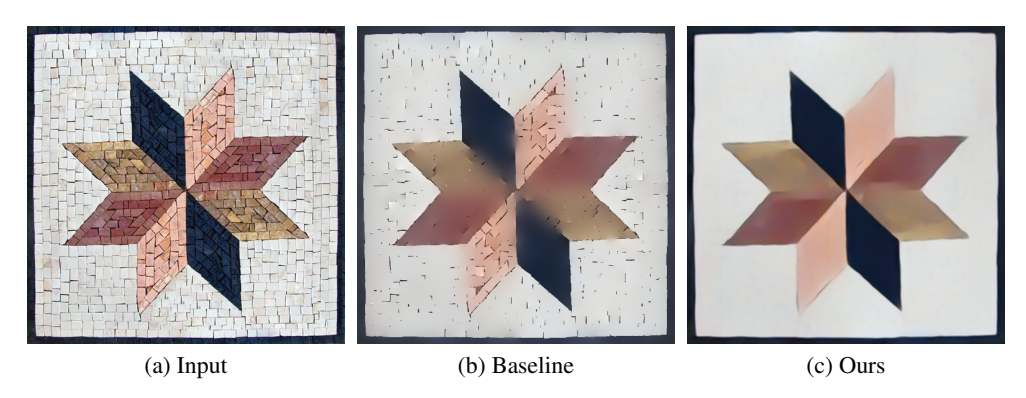


Figure 8: Ablation study on loss functions. (a) Input, (b) Baseline means $\lambda_1 = 0$ in equation 15. (c) Full total loss.

B ADDITIONAL ABLATION STUDIES

Visual ablattion results of λ_1, λ_2 . Figure 8 presents the ablation results. As shown in Figure 8(b), the baseline struggles to control smoothing intensity, leading to residual textures and oversmoothed edges. In contrast, Figure 8(c) shows that our GELR model, optimized via ADMM, effectively adjusts the smoothing level, producing cleaner and more structurally consistent results. Furthermore, GELR enable RPAFNet to flexibly balance smoothing and detail preservation. We have reported different values of λ_1, λ_2 impact on filtering performance in Table 5. The best choice of λ_1, λ_2 is 0.7, 0.3.

Table 5: Quantitative results of different values for λ_1, λ_2 .

(λ_1, λ_2)	(0.1,0.9)	(0.2,0.8)	(0.3,0.7)	(0.4,0.6)	(0.5,0.5)
BRISQUE↓	50.265	48.960	45.045	42.571	39.540
$\mathbf{NIQE}\downarrow$	9.472	8.352	7.827	7.012	6.846
(λ_1,λ_2)	(0.6,0.4)	(0.7,0.3)	(0.8,0.2)	(0.9,0.1)	(1.0,0)
BRISQUE↓	34.254	30.041	36.415	40.176	45.251
NIQE↓	6.512	5.972	6.480	7.091	8.273

CTUM ablation results. It enables the fusion of both local and global representations, thereby enriching the feature space. This design allows the model to better reconstruct fine details while maintaining global coherence, resulting in more visually detailed outputs. We have reported quantitative results of the ablation experiment for the CTUM, as shown in Table 6.

Table 6: Quantitative results of ablation study on CTUM module.

Networks	Metrics	BRISQUE↓	PIQE↓	NIQE ↓
Baseline	w/o	28.537	51.698	8.631
RPAFNet	W	21.665	30.275	4.307

C APPLICATION EXPERIMENTS

To further illustrate the proposed model's performance, we utilize three downstream tasks to compare our approach against the state-of-the-art methods, across three smoothing applications, which include details manipulation, image stylization and clipart compression artifact filtering.

C.1 DETAILS MANIPULATION.

It enhances details by incorporating multiple texture layers, extracted by subtracting the smoothed image from the original. We present details manipulation results of different SOTA techniques in

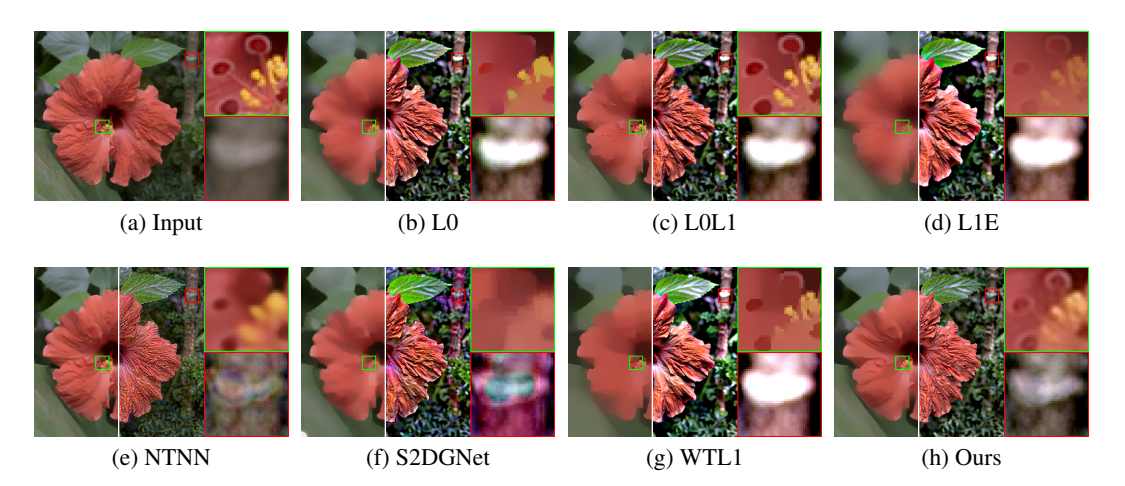


Figure 9: Details Manipulation. (a) The input image. It is enhanced with four details layers via SOTA methods: (b) L0, (c) L0L1, (d) L1E, (e) NTNN, (f) S2DGNet, (g) WTL1, (h) Ours. The right green enlarged area denotes the details of smoothed image, and the red-marked enlarged boxes are corresponding enhanced details. From these marked areas, one can see that our method can reduce halo artifacts. Meanwhile, it keeps more edges than other algorithms.

Figure 9. The left part of each image is the smoothed image, while the right parts are corresponding detail enhanced images. Green enlarged areas show details from smoothed results and red enlarged areas reveal details from enhanced images. L0, L1E and S2DGNet oversmoothed edges in green marked boxes. L0L1, NTNN, and WTL1 obtained competive edges. However, L0, L0L1, L1E and WTL1 suffer white halo artifacts, and also NTNN, S2DGNet produce colorful halo artifacts. In contrast, the proposed model obtains the best visual effect, which reduces significant halo artifacts.

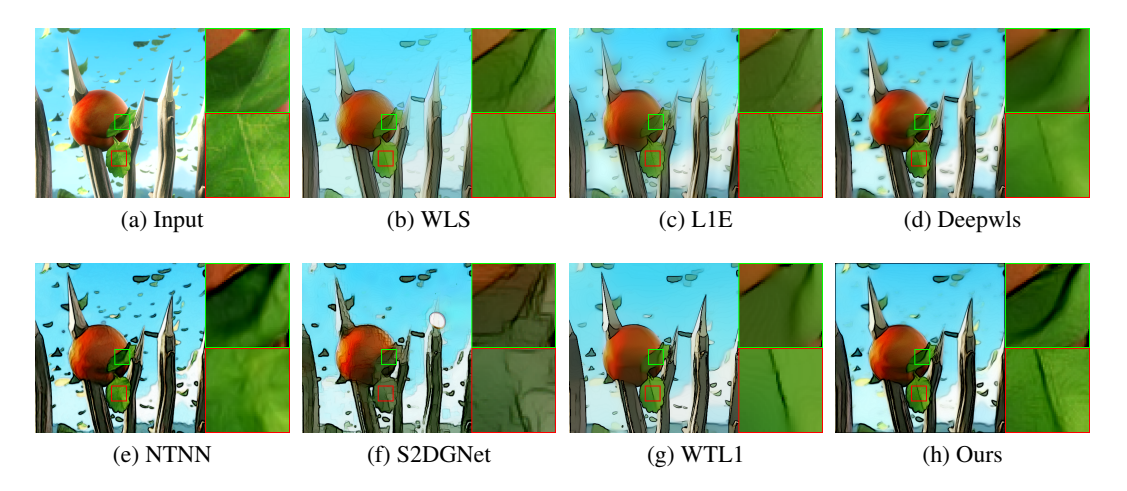


Figure 10: Image stylization. (a) The input image, stylization results of (b) WLS, (c) L1E, (d) Deepwls, (e) NTNN, (f) S2DGNet, (g) WTL1, (h) Ours. From these marked and enlarged areas, one can see that our model has significant advantages in the main structures preserving.

C.2 IMAGE STYLIZATION.

This task aims to transform an input image into an image with new style, while preserving the main contents. This technique can abstract the content of low-contrast areas while preserving the high-contrast features of images. Stylization results of the comparison approaches are shown in Figure 10. It is worth noting that WLS, L1E, Deepwls, and NTNN can not preserve the high-contrast edges, leading to oversmoothing. We recommend focusing on these green and red highlighted ar-

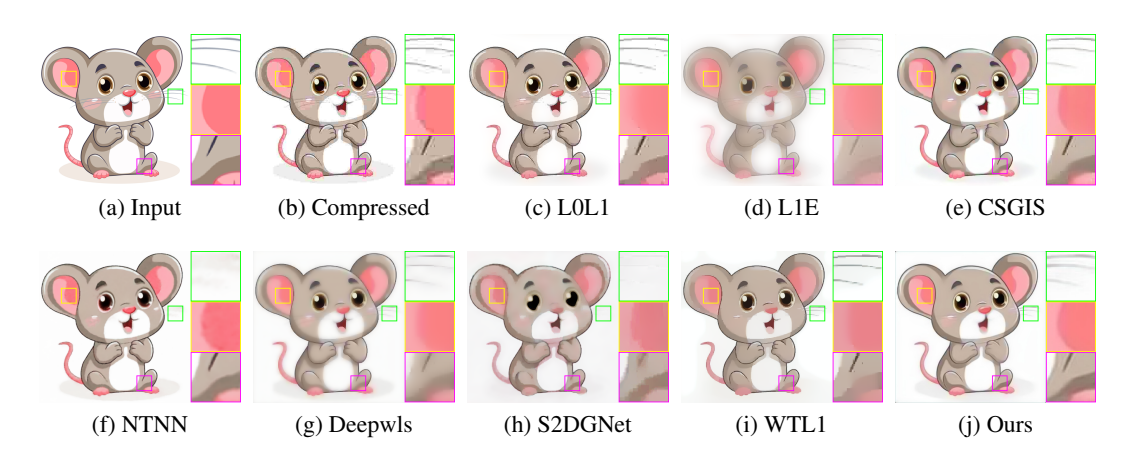


Figure 11: Clip-arts JPEG artifacts filtering. (a) Given input image, (b) The compressed image. It is smoothed by (c) L0L1, (d) L1E, (e) CSGIS, (f)NTNN, (g) Deepwls, (h) S2DGNet, (i) WTL1, and (j) Ours. Referring to the marked boxes, (c), (d), (f), (g) and (h) suffer from blurred edges. (e) and (i) filter artifacts uncleanly.

Table 7: PSNR (dB) and SSIM comparison for artifacts filtering.

Methods	L0L1	L1E	CSGIS	Deepwls
PSNR	27.86	20.63	27.03	24.46
SSIM	0.8931	0.8460	0.8912	0.8889
Methods	NTNN	S2DGNet	WTL1	Ours
PSNR	27.88	22.81	24.66	28.67
SSIM	0.8935	0.8640	0.8122	0.9151

eas. S2DGNet and WTL1 obtain competitive performance, while they also can not do the best in emphasizing high-contrast structures. By contrast, the proposed model has a significant superiority in structure keeping and obtains the best visual effects over the compared techniques.

C.3 ARTIFACTS FILTERING.

The technique of compression artifacts filtering aims to be employed to eliminate JPEG block artifacts when converting clip-art images into JPEG format. When an image is compressed at a low bit rate using standard JPEG encoding, compression artifacts often manifest along sharp edges, while staircase artifacts may arise in homogeneous regions. In this study, a 10% compression rate is applied to the given clip-art image. Figure 11 illustrates the smoothed results obtained from various SOTA models. It is evident that L1E, Deepwls blur the input image. L0L1, CSGIS, and WTL1 filter the JPEG blocks uncleanly. Meanwhile, L0L1 and S2DGNet also produce staircase edges. NTNN and S2DGNet oversmoothed the details of the input image, referring to contents of the green enlarged boxes. However, the proposed method keeps better edges and details while removing JPEG block artifacts cleanly. We also show the numerical PSNR and SSIM values corresponding to this task in Table 7. Our proposed model demonstrates the best performance, achieving the highest PSNR value of 28.67 and an SSIM value of 0.9151. Whatever the visual effects or quantitative numerical metrics, the proposed model achieves the best performance against other SOTA methods in the removal of compression artifacts.

C.4 EXPERIMENTS ON PUBLIC DATASETS

We conduct smoothing experiments across on the three public datasets, including SPS (Feng et al., 2021), NKS (Xu et al., 2020), and ECS (Qi et al., 2024), three above datasets have paired ground-truth smoothed images. The smoothed images are shown in Figure 12. The first row of images are from NKS dataset, the second row of images are from SPS dataset, and the last row of images are from ECS dataset. For these results of NKS dataset, L1E, Deepwls, and WTL1 suffer from blurring

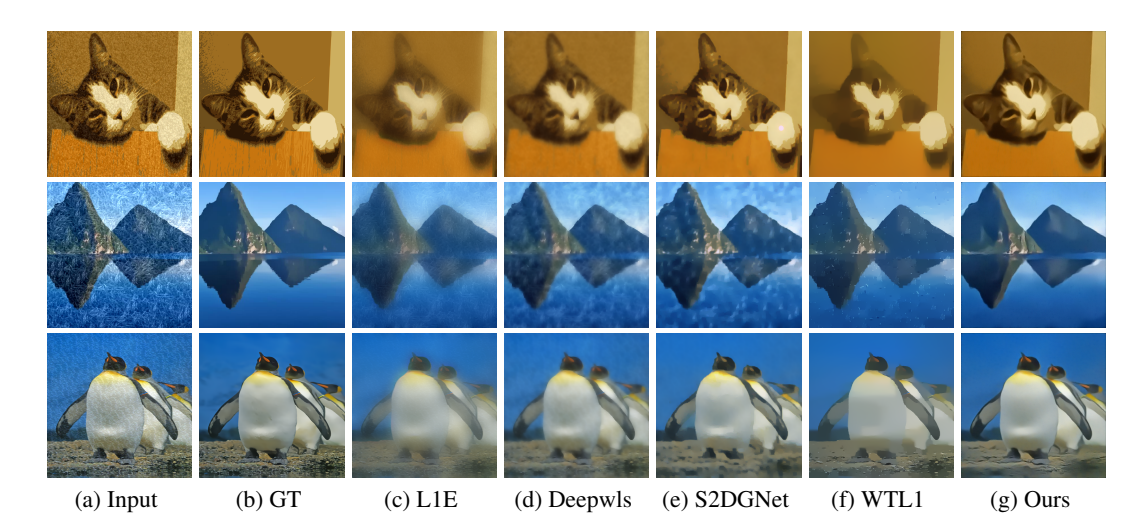


Figure 12: Image smoothed results across three datasets. (a) The input images, filtered by (c) L1E, (d) Deepwls, (e) S2DGNet, (f) WTL1, (g) Ours, and corresponding their (b) GT. The first row of images are from NKS dataset, the second row of images are from SPS dataset, and the last row of images are from ECS dataset. It is evident that L1E, Deepwls blur output images, while Deepwls, S2DGNet and WTL1 filter textures uncleanly. In contrast, the proposed model obtain the best visual effect across three datasets, demonstrated the robustness of our technique.

Table 8: PSNR(dB) and SSIM values across three public datasets.

Methods	Datasets					
-	NKS		SPS		ECS	
	PSNR	SSIM	PSNR	SSIM	PSNR	SSIM
L0 (2011)	27.36	0.8932	27.85	0.8826	25.37	0.8539
L0L1 (2022)	25.60	0.8425	26.21	0.8633	24.58	0.7946
L1E (2022)	26.15	0.8651	24.68	0.8295	25.14	0.8021
ILS (2020)	25.98	0.8863	25.57	0.8413	23.25	0.7488
QWLS (2024)	28.27	0.8924	27.57	0.8739	25.16	0.8049
SEMF (2023)	28.46	0.8962	27.71	0.8892	24.75	0.7983
WLS (2008)	23.56	0.8014	24.56	0.8541	22.89	0.8014
CSGIS (2022)	34.50	0.9486	24.56	0.8541	24.90	0.8701
E2H (2021)	34.24	0.9401	31.73	0.9202	26.89	0.8914
Deepwls (2023)	27.63	0.8876	26.55	0.8798	24.87	0.8153
NTNN (2024)	29.89	0.9035	28.57	0.9024	26.49	0.8849
S2DGNet (2024)	33.76	0.9503	32.15	0.9302	30.45	0.9101
WTL1 (2024)	25.43	0.8519	26.47	0.8718	24.76	0.7395
Ours	34.98	0.9575	32.68	0.9382	31.68	0.9286

and over-smoothing to varying degrees. S2DGNet obtains competitive filtering results. For these ouputs of SPS dataset, the all compared techniques filter textures uncleanly. For these smoothed images of ECS dataset, It is evident that L1E, Deepwls blur output images, while S2DGNet and WTL1 over-smoothing details. In contrast, the proposed model obtain the best visual effect across three datasets, demonstrated the robustness of our technique. The corresponding numerical values of PSNR and SSIM are presented in Table 8. It is evident that our model achieves the best index in smoothing on three public datasets.